Journal of Electroceramics, 14, 149–156, 2005

The Role of Oxygen Vacancies on the Microstructure Development and on the Electrical Properties of SnO_2-Based Varistors

R. PARRA,[1,*] C.M. ALDAO,[1] J.A. VARELA[2] & M.S. CASTRO[1]

[1] *Institute of Materials Science and Technology (INTEMA, CONICET-UNMdP), J.B. Justo 4302, B7608FDQ - Mar del Plata, Argentina*
[2] *Instituto de Química, UNESP; PO Box 355, 14801-970 - Araraquara, SP, Brazil*

Submitted April 13, 2004; Revised August 27, 2004; Accepted August 31, 2004

Abstract. Variations on the microstructure development and on the electrical properties of SnO_2-based varistors are discussed on the basis of the oxygen vacancies created or annihilated by the presence of different additives. Electron paramagnetic resonance (EPR) analysis of sintered samples evidenced a substantial increase in the paramagnetic oxygen vacancies concentration when Nb_2O_5 is added to the $SnO_2 \cdot Co_3O_4$ system. On the other hand, the observed diminution in the concentration of such species after the addition of Fe_2O_3 indicates solid solution formation. The quantification of paramagnetic oxygen vacancies allowed to confirm the proposed substitutions taking place in the lattice during sintering. These findings are supported by scanning electron microscopy, by density measurements and by current density versus electric field curves. The characterization of secondary phases through EDS assisted SEM and TEM is also reported in this work.

Keywords: defects, electrical properties, microstructure, varistors, EPR

1. Introduction

Metal oxide varistors are electronic ceramic devices whose function is to sense and limit transient voltage surges and to do so repeatedly without being destroyed or damaged [1, 2]. Their non-linear current-voltage behavior is properly described by the equation $I = V^{\alpha}$, where α is the non-linearity coefficient whose magnitude is strongly influenced by the addition of transition metal oxides to the varistor composition [3, 4].

Tin dioxide is an *n*-type wide band gap semiconductor with a very low densification rate due to its high surface diffusion at low temperatures and high SnO_2 partial vapour pressure at sintering temperatures [5]. Pianaro et al. reported a significant improving in the sinterability of SnO_2 by doping it with Co_2O_3 and Nb_2O_5 [6]. The SnO_2-based varistor system doped with Co_3O_4 or MnO_2 among other oxides presents a simple single phase structure under X-ray resolution in which Sn^{+4} ions are replaced by Mn^{+3}, Mn^{+2}, Co^{+3} or Co^{+2} ions giving place to a solid solution and to the creation of oxygen vacancies at sintering temperatures [7, 8]. Oxygen vacancies, both paramagnetic and diamagnetic, have been determined to be the major promoters of SnO_2 densification for they activate solid state diffusion and mass transport mechanisms that lead to material densification and grain growth [9, 10]. On the other hand, Nb_2O_5 and Sb_2O_3 have a detrimental effect on the sinterability of SnO_2 [9, 11, 12].

The purpose of the present work is to consider the influence of different additives in the concentration of oxygen vacancies, and their effect on the microstructure development and on the electrical properties of SnO_2-based varistors. The lattice distortion, consequence of the solid solution formation, and the occurrence of secondary phases are also discussed to gain knowledge of the variables that affect the varistor behavior.

2. Experimental Procedure

Analytical grades of SnO_2 (Aldrich), Co_3O_4 (Merck), Nb_2O_5 (Fluka AG), and Fe_2O_3 (Baker) were used as

*E-mail: rparra@fi.mdp.edu.ar

Table 1. Sample composition (%mol)

Sample	SnO_2	Co_3O_4	Nb_2O_5	Fe_2O_3
S	100.0	–	–	–
SC	99.670	0.33	–	–
SCN	99.645	0.33	0.025	–
SCN-0.025%Fe_2O_3	99.620	0.33	0.025	0.025
SCN-0.050%Fe_2O_3	99.595	0.33	0.025	0.050

precursors for processing SnO_2-based varistors. Selected compositions are listed in Table 1. After mixing the powders in an alcoholic medium by stirring with a high-speed turbine at 6000 rpm for 5 minutes, the slurries were kept at 65 ˚C for 48 hours. Mixtures were sieved through a 43 μm mesh screen and the granulated powders pressed into discs by uniaxial pressing (80 MPa) followed by isostatic pressing (200 MPa). Finally, the pellets were sintered in air within a Pt box at 1300˚C for 2 hours with heating and cooling rates of 3˚C/minute. In order to minimize or avoid Co loss during sintering and to ensure the desired composition, pellets were covered with their own powder.

The apparent density of sintered samples was estimated by the Archimedes method. X-ray powder diffraction (XRD) analysis was carried out with a Rigaku 22000 equipment running with CuK_α radiation. Microstructural characterizations of the samples were performed by scanning electron microscopy (SEM), in a Topcon SM-300 microscope over polished samples, and by transmission electron microscopy (TEM), in a Philips CM200 instrument operating at 200 kV. Both SEM and TEM instruments were equipped with an EDS (PGT PRISM-Digital Spectrometer) system for energy dispersive X-ray analysis. Mean grain sizes were estimated from SEM micrographs through the method of the interceptions proposed by Mendelson [13].

A Bruker ER-200 (Band X) EPR spectroscope was used in order to characterize the paramagnetic species present in the systems. The EPR signal intensities were arranged as double integrated intensities (DII) calculated from the expression proposed by Murugaraj et al. [14].

$$DII = \frac{hw^2}{mGA\sqrt{P}}, \tag{1}$$

where h and w are the signal height and width respectively, m is the sample mass, G the gain, A the amplitude modulation and P the power.

Sintered samples were lapped to ensure plane parallel faces where silver electrodes were deposited for electrical characterization. A Keithley 237 high voltage source—measure unit was used to acquire plots of the current density J as function of the electric field E. The electrical breakdown field was obtained at 1 mA·cm^{-2} current density and the voltage per barrier v_b was estimated as

$$v_b = \frac{E_r}{n}, \tag{2}$$

where E_r is the electrical breakdown field and n is the number of grains of a given sample of width L and mean grain size d,

$$n = \frac{L}{d}. \tag{3}$$

The electrical breakdown field was also measured at 10 mA·cm^{-2} to consider those samples that do not reach the breakdown region at 1 mA· cm^{-2}.

The nonlinear coefficient α was estimated from room temperature J-E curves by Eq. (4),

$$\alpha = 1/\log(E_{10\text{mA}}/E_{1\text{mA}}), \tag{4}$$

where $E_{10\text{mA}}$ and $E_{1\text{mA}}$ are the electric fields at current densities of 10 mA·cm^{-2} and 1 mA·cm^{-2}, respectively.

3. Results and Discussion

Table 2 shows the densities of the sintered samples obtained through the Archimedes method.

The addition of Co_3O_4 to SnO_2 induced modifications in the oxygen vacancies concentration responsible for the high densities attained. On the contrary, Nb_2O_5 produced a negligible effect on the samples

Table 2. Relative density (ρ_r), mean grain size (d), breakdown electric field (E_r), non-linear coefficient (α) and grain breakdown voltage (v_b) of sintered samples.

Sample	ρ_r (%)	d (μm)	$E_{r;1\text{mA}}$ (V/cm)	$E_{r;10\text{mA}}$ (V/cm)	α	$v_{b;1\text{mA}}$ (V/grain)
S	58.7	0.90	–	–	–	–
SC	97.9	5.08	6460	8820	7	3.2
SCN	97.8	4.06	2100	3540	4	0.9
SCN-0.025%Fe_2O_3	98.5	4.52	4200	5130	12	2.0
SCN-0.050%Fe_2O_3	98.5	6.93	6570	7180	26	4.3

SnO_2 theoretical density: 6.95 g·cm^{-3}

density; however, higher density values were achieved with small additions of Fe_2O_3. In order to explain these changes, replacement equations in the tin oxide lattice are discussed as follows. With the addition of Co_3O_4 the possible substitution equations, where the Kröger-Vink standard notation is used, are:

$$Co_3O_4 \rightarrow CoO + Co_2O_3 \quad (5)$$

then,

$$CoO \rightarrow Co''_{Sn} + V^{\cdot\cdot}_O + O^x_O \quad (6)$$

$$CoO \rightarrow Co''_{Sn} + 2V^{\cdot}_O + \frac{1}{2}O_2 \quad (7)$$

$$Co_2O_3 \rightarrow 2Co'_{Sn} + V^{\cdot\cdot}_O + 3O^x_O \quad (8)$$

$$Co_2O_3 \rightarrow 2Co'_{Sn} + 2V^{\cdot}_O + 2O^x_O + O_2 \quad (9)$$

$$V^{\cdot\cdot}_O + e' \rightarrow V^{\cdot}_O. \quad (10)$$

Cobalt ions bring about an increase in the oxygen vacancies concentration allowing solid state diffusion and material densification. In the Nb_2O_5 addition the following equations may apply.

$$2Nb_2O_5 \rightarrow 4Nb^{\cdot}_{Sn} + V''''_{Sn} + 10O^x_O \quad (11)$$

$$V''''_{Sn} + 2V^{\cdot\cdot}_O \rightarrow 2V^{\cdot}_O + V''_{Sn}, \quad (12)$$

or

$$Nb_2O_5 \rightarrow 2Nb^{\cdot}_{Sn} + 2e' + 4O^x_O + \frac{1}{2}O_2 \quad (13)$$

$$V^{\cdot\cdot}_O + e' \rightarrow V^{\cdot}_O. \quad (14)$$

Then, Nb_2O_5 is not expected to improve the densification of sample SC since it does not create new V_O species. Niobium oxide is an electron donor that increases the electrical conductivity of SnO_2. The electrons introduced through Eq. (13) may be involved in the transformation of $V^{\cdot\cdot}_O$ into $V^{\cdot}_O$. In the Fe_2O_3 addition the substitution equations are:

$$Fe_2O_3 \rightarrow 2Fe'_{Sn} + V^{\cdot\cdot}_O + 3O^x_O \quad (15)$$

$$Fe_2O_3 \rightarrow 2Fe'_{Sn} + 2V^{\cdot}_O + 2O^x_O + O_2 \quad (16)$$

$$FeO \rightarrow Fe''_{Sn} + V^{\cdot\cdot}_O + O^x_O \quad (17)$$

$$V^{\cdot\cdot}_O + e' \rightarrow V^{\cdot}_O. \quad (18)$$

From Table 2, Fe_2O_3 addition to the SCN system produced a higher density material due to the further creation of oxygen vacancies.

Table 3. Lattice parameters of the sintered samples.

Sample	a (Å)	c (Å)	V (Å^3)
S	4.720	3.179	70.81
SC	4.721	3.180	70.87
SCN	4.716	3.175	70.63
SCN-0.025%Fe_2O_3	4.712	3.177	70.53
SCN-0.050%Fe_2O_3	4.708	3.170	70.26

The X-ray powder diffraction patterns of the different systems showed no other phase besides cassiterite, suggesting single phase systems within the detection limits of this technique. Lattice parameters listed in Table 3 exhibit the effect on the unit cell dimensions of the foreign ions when constituting a solid solution. These changes, which are influenced by the valence in which the ion is stabilised in the lattice, can be explained from the substitution equations above. There exists the possibility for cobalt to stabilise as Co^{+2} (ionic radius 0.72 Å) or as Co^{+3} (0.63 Å); in agreement with previous studies [15], we have confirmed its stabilization mainly as Co^{+2}, an ion greater in volume than Sn^{+4} (0.71 Å). Should Co^{+3} be the dominant species, a decrease in the unit cell volume would be certainly measured. A shrinkage in the cell volume was expected with the addition of Nb_2O_5 to the SC system due to the lower ionic radius of Nb^{+5} (0.69 Å) with respect to that of Sn^{+4}. A diminution in the lattice parameters was also measured when Fe_2O_3 was added to the varistor composition. The same trend observed after increasing the amount of this oxide indicates the preferred stabilisation of iron as Fe^{+3} (0.64 Å) against the more voluminous Fe^{+2} (0.74 Å). Similar results on the unit cell volume were obtained by Antunes et al. adding Fe_2O_3 to a $SnO_2{\cdot}CoO{\cdot}Nb_2O_5$ system [16].

Mean grain sizes in Table 2 confirm grain growth inhibition when Nb_2O_5 is added to the SC system. The reduction in the mean grain size is explained through Eq. (11) to (14); the phenomenon is ascribed to the annihilation of oxygen vacancies produced during the Sn^{+4} replacing by Nb^{+5}. A remarkable grain growth and the highest density material were achieved after increasing the Fe_2O_3 content of the SCN-0.025%Fe_2O_3 sample, which are associated to the creation of additional oxygen vacancies. An opposed effect in systems with even higher Fe_2O_3 concentrations, revealing a grain growth inhibition due to iron oxide segregation at grain boundaries, was formerly reported [16].

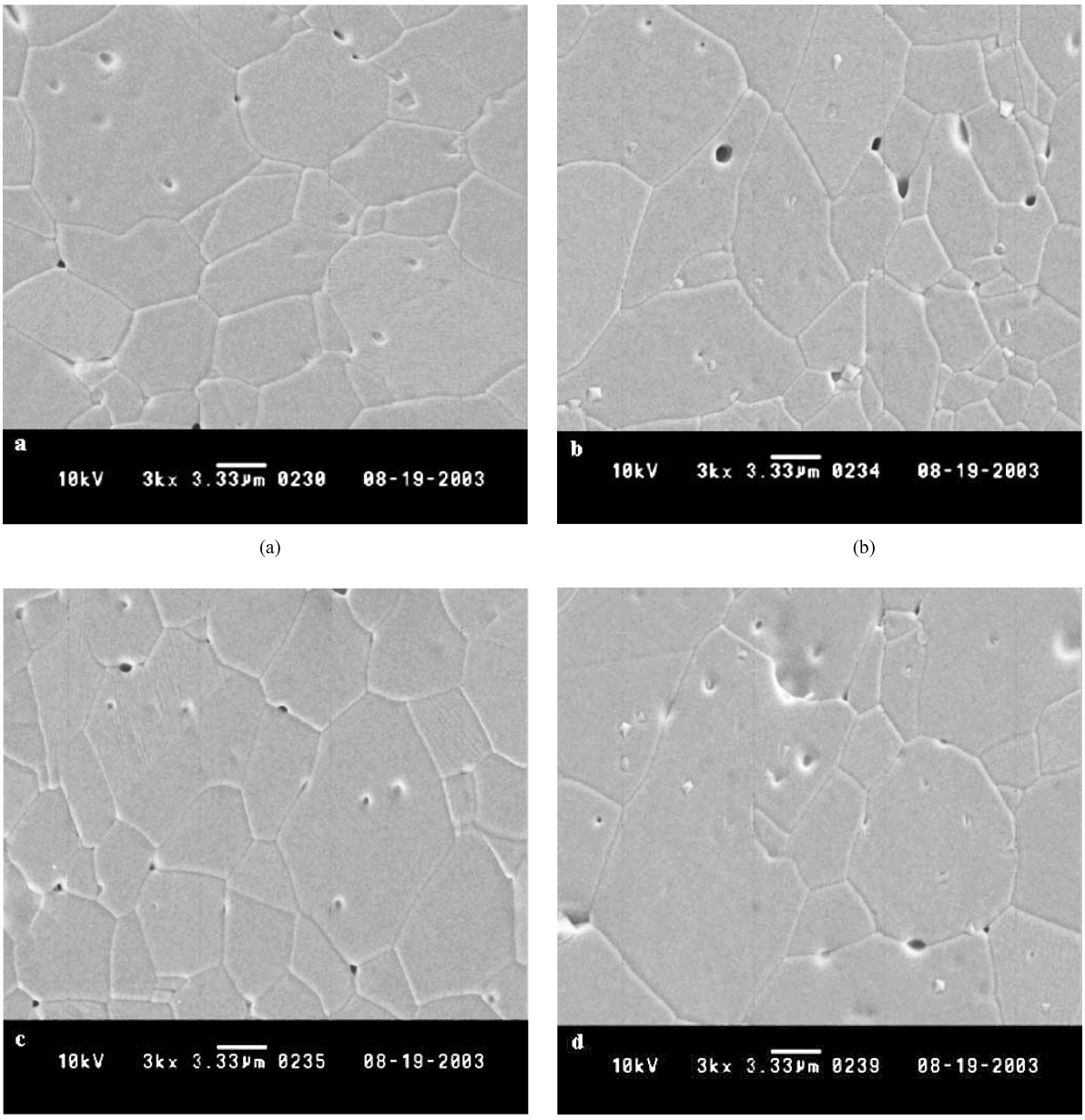

(a) (b)

(c) (d)

Fig. 1. SEM micrographs of samples sintered at 1300°C for 2 hours: (a) SC; (b) SCN; (c) SCN-0.025%Fe_2O_3; (d) SCN-0.050%Fe_2O_3.

Contrary to the observations derived from the XRD patterns, the occurrence of secondary phases was evidenced through SEM analysis as shown in Figs. 1(b) and (d). The composition of the different phases was determined with EDS facilities attached to the microscope. Figure 2(a) is shown as the representative plot of the results obtained for the grain regions in SC, SCN and iron doped samples; only the signals that belong to SnO_2 were recorded. Figures 2(b) and (c) show those peaks corresponding to the precipitates observed in samples SCN and SCN-0.050%Fe_2O_3 respectively; the EDS analysis revealed the presence of Sn and Co

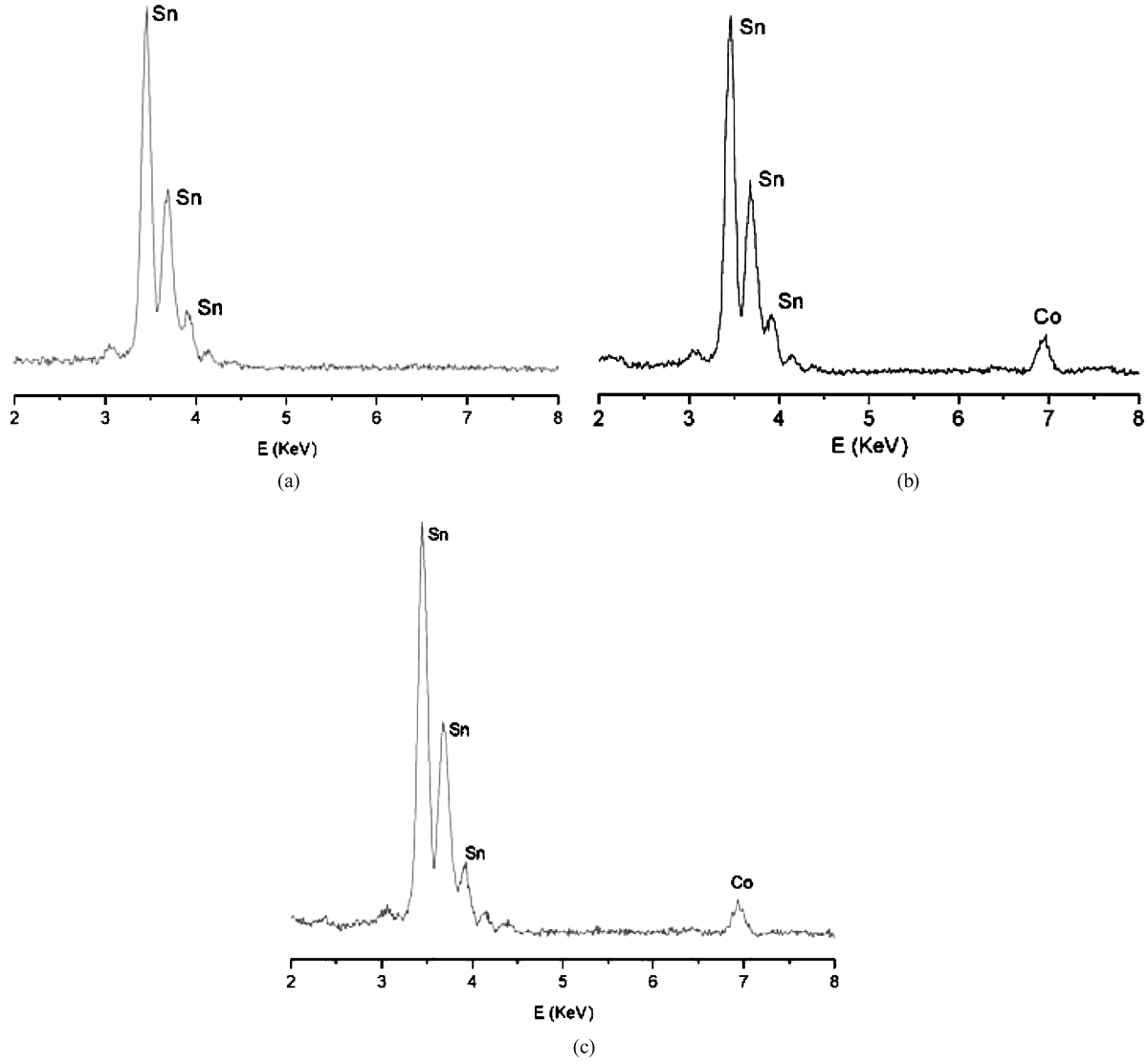

Fig. 2. EDS analysis from SEM images in Fig. 1. (a) grain region; (b) precipitate in SCN; (c) precipitate in SCN-0.050%Fe_2O_3.

in the composition of the precipitates found in both systems. Although no precipitates are visible in the SEM image of the SCN-0.025%Fe_2O_3 sample, secondary phases are also present in such system. Furthermore, smaller precipitates of different composition ($Co_{1.5}FeSn_{0.5}O_4$) were unveiled through TEM in SCN-0.050%Fe_2O_3 samples as shown in Fig. 3(a) and discussed in a previous study [17]. Figures 3(b) and (c) show the EDS analysis corresponding to the grain region and to the secondary phases observed. Under the assumption of few Nb^{+5} ions effectively replacing Sn^{+4} in the lattice when Fe^{+3} is present, Nb_2O_5 excess might therefore be precipitated or segregated towards the grain boundaries. Even so, niobium was not found whether in the grains or in the precipitates composition; we believe it is simply due to the detection limits of the EDS technique and to the low percentage of niobium oxide employed. Oliveira et al. showed the presence of Nb in the composition of the secondary phases present in the $SnO_2{\cdot}CoO{\cdot}Nb_2O_5{\cdot}Pr_2O_3$ system, even where Nb^{+5} is one of the two species with high probability of replacing Sn^{+4} in the lattice [18].

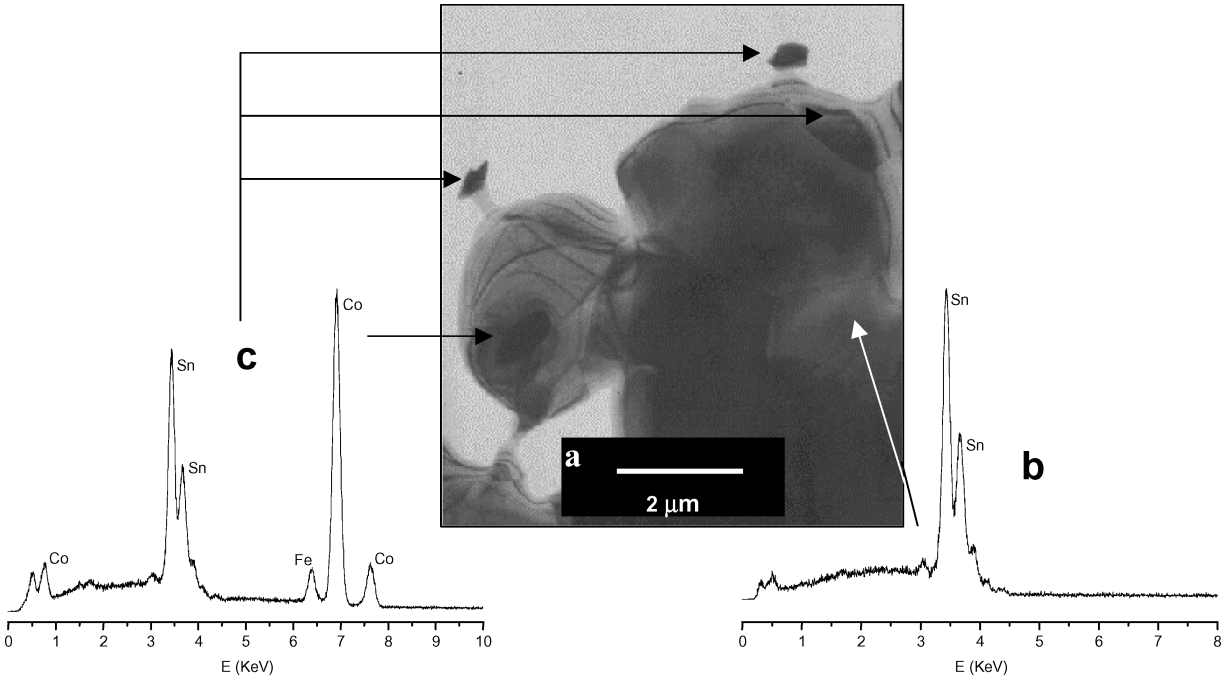

Fig. 3. TEM micrograph of the SCN-0.050%Fe_2O_3 system showing the secondary phases present and EDS analysis of the (b) grain region and (c) precipitates.

Table 4 lists EPR double integrated intensities of the paramagnetic oxygen vacancies ($V_O^{\cdot}$) signal [19] on sintered and grounded samples. While EPR analysis is done at low temperature, oxygen vacancies are created at high temperatures in the course of sintering. During the cooling process, a non-uniform distribution of defects is established because of diffusion phenomena and the final defects concentration is lower near the surface than in the bulk of the grain [20]. Therefore, the concentration and profile of defects at room temperature must be substantially different than what happens at sintering temperatures. However, the results in Table 4 are representative of the effect of the additives employed, for this difference in the defects concentration is shared by every sample treated under the same sintering conditions.

Table 4. Relative EPR double integrated intensities (DII) of $V_O^{\cdot}$(g = 1.89 [19]) for sintered and grounded samples.

Sample	DII ($V_O^{\cdot}$) / $DII_{sample\text{-}S}$ ($V_O^{\cdot}$)
S	1.0
SC	5.3
SCN	2702.0
SCN-0.025%Fe_2O_3	495.0
SCN-0.050%Fe_2O_3	154.1

An exceptional increase in the concentration of the $V_O^{\cdot}$ species is observed when Nb_2O_5 is added to the SC sample. This phenomenon accounts for the turning of $V_O^{\cdot\cdot}$ into $V_O^{\cdot}$ according to Eqs. (12) and (14). When Fe_2O_3 is included within the additives, a decrease in the $V_O^{\cdot}$ signal is observed. Interestingly enough, with the addition of iron oxide there is an increase in the material density that undoubtedly stands for the further creation of oxygen vacancies ($V_O^{\cdot\cdot}$ and/or $V_O^{\cdot}$). However, contrary to our expectations, their EPR signal intensity is neither higher nor equal to that of the SCN samples, but lower, implying that the concentration of $V_O^{\cdot}$ is being somehow depressed. The main event responsible for the arising of paramagnetic oxygen vacancies is the substitution of Sn^{+4} for Nb^{+5}; but, by virtue of the difference between the ionic radii of Fe^{+3} and Nb^{+5}, there exists a higher probability for Sn^{+4} to be substituted by Fe^{+3}. Then, the transformation of $V_O^{\cdot\cdot}$ into the paramagnetic species $V_O^{\cdot}$ is inhibited in the presence of Fe_2O_3 by the lack of the electrons required in

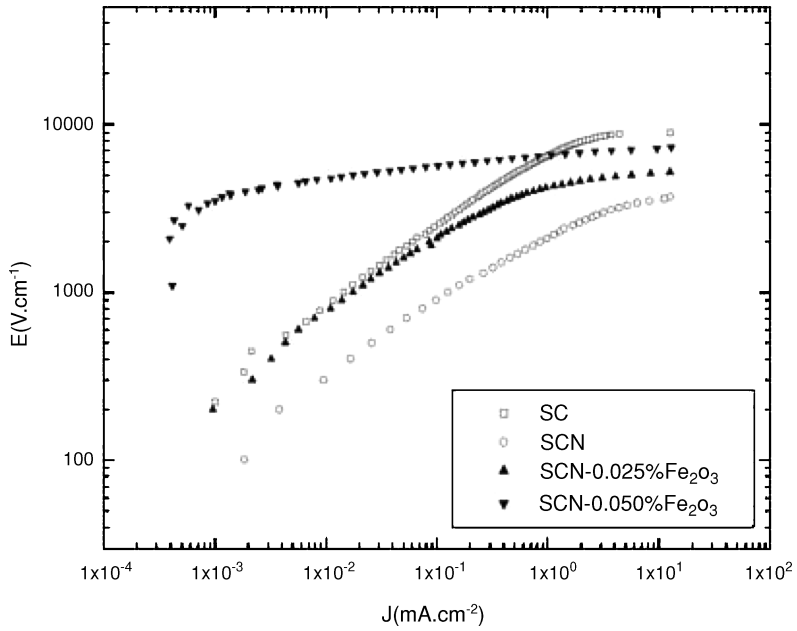

Fig. 4. *J-E* characteristic curves of sintered samples at room temperature.

the process; consequently, the creation of paramagnetic oxygen vacancies is restrained and the observation of a lower intensity $V_O^{\cdot}$ signal for iron doped samples hence clarified. The former discussion is also supported by the lower conductivity and higher breakdown voltage of Fe_2O_3-doped specimens compared to those of the SCN sample.

In Fig. 4 we present the room temperature *J-E* curves obtained for the different compositions studied. Sample SC displayed a high ceramic resistance which was controlled with the addition of Nb_2O_5 since niobium oxide acts as an electron donor [6, 9]. The most remarkable effect of the Fe_2O_3 addition over the SCN system was to increase both the breakdown voltage and the non-linear coefficient α as shown in Table 2. The greater likelihood of iron against niobium to substitute the host ion in the lattice is responsible for precluding the release of electrons and $V_O^{\cdot}$ during the Nb^{+5}/Sn^{+4} substitution and for the higher overall resistance of the system thereafter. We consider that the rise in the breakdown voltage per barrier, v_b, when the Fe_2O_3 concentration is increased might be due to its segregation to grain boundaries. Moreover, the enhancement of the non-linear properties of these devices is commonly attributed to the segregation of trivalent metal oxides to grain boundaries where they induce changes in the concentration of the atomic defects at grain-grain interfaces [18]. Assuming a Schottky type electrical barrier at SnO_2 grain boundaries, the negative surface charge at the interface separating two grains is compensated by the positive charge in the depletion layers in the grains on both sides of the interface [3]. This atomic defects model involves positively charged donors ($V_O^{\cdot\cdot}$, $V_O^{\cdot}$, $Nb_{Sn}^{\cdot}$) located at the depletion layers and negatively charged acceptors (Fe_{Sn}'', Fe_{Sn}', Co_{Sn}', Co_{Sn}'', V_{Sn}'', V_{Sn}'''', O', O'') at the grain boundaries interface. Deep negatively charged species at intergrains contribute to the potential barrier height and, since there is an increase in the non linear coefficient α in samples SCN-0.025%Fe_2O_3 and SCN-0.050%Fe_2O_3, an enhanced barrier height is inferred in these systems. On the other hand, the increase in the donors concentration ($V_O^{\cdot\cdot}$) should be reflected in a higher conductivity due to tunnel effect currents; however, this is counterbalanced by the simultaneous increase in the potential barrier height since the concentration of negatively charged species is also being increased. Although a low concentration level of precipitates was found in the specimens studied, the occurrence of secondary phases that concentrate the additives is a further factor that may modify the expected electrical properties. Simões et al. suggested the presence of an excessive amount of precipitates to be

deleterious to the non-ohmic properties of SnO_2-based varistor devices [21].

4. Conclusions

The experimental results here reported highlight the influence of oxygen vacancies in the overall properties of SnO_2-based varistors. The following conclusions are thereby derived.

1. When replacing Sn^{+4} in the lattice, Co^{+2} and Fe^{+3} ions activate solid state diffusion mechanisms via the creation of oxygen vacancies that stimulate the densification of SnO_2 attaining near-theoretical density values.
2. The presence of secondary phases concentrating the additives and localized inside the grains and at boundary regions were unveiled with SEM and TEM analysis.
3. Through EPR studies of the variations in the paramagnetic oxygen vacancies signal, the replacement of Sn^{+4} by Fe^{+3} was determined. This statement is validated by ionic radii data, by mean grain sizes and by the higher resistance of Fe_2O_3-doped samples.
4. A varistor device with the highest non-linear coefficient was obtained by adding 0.050% mol of Fe_2O_3 to a typical $SnO_2{\cdot}Co_3O_4{\cdot}Nb_2O_5$ system.

Acknowledgments

The authors are highly grateful to the Programa CYTED (Proyecto PI-VIII.13 PROALERTA), to Fundación Antorchas and CONICET (Argentina), to CNPq and FAPESP (Brazil) for the financial support provided for this research. The cooperation of the personnel at the IQ, Araraquara, is also acknowledged.

References

1. L.M. Levinson and H.R. Philipp, *Am. Ceram. Soc. Bull.,* **65**, 639 (1986).
2. M. Matsuoka, in *Grain Boundary Phenomena in Electronic Ceramics, Advances in Ceramics*, Vol. 1, edited by L.M. Levinson (The American Ceramic Society Inc., Ohio, 1981), p. 290.
3. T.K. Gupta, *J. Am. Ceram. Soc.*, **73**, 1817 (1990).
4. S.A. Pianaro, P.R. Bueno, E. Longo, and J.A. Varela, *Ceram. Inter.*, **25**, 1 (1991).
5. S.A. Pianaro, P.R. Bueno, P. Olivi, E. Longo, and J.A. Varela, *J. Mat. Sci. Lett.*, **16**, 634 (1997).
6. S.A. Pianaro, P.R. Bueno, E. Longo, and J.A. Varela, *J. Mat. Sci.Lett.*, **14**, 692 (1995).
7. M.S. Castro and C.M. Aldao, *J. Eur. Ceram. Soc.*, **18**, 2233 (1998).
8. C. Li, J. Wang, W. Su, H. Chen, W. Wang, and D. Zhuang, *Physica B*, **307**, 1 (2001)
9. J.A. Varela, L.A. Perazolli, E. Longo, E.R. Leite, and J.A. Cerri, in *Radiation Effects & Defects in Solids* (Gordon and Breach Science Publishers, India, 1998), Vol. 146, p. 131.
10. P.R. Bueno, E.R. Leite, L.O.S. Bulhões, E. Longo, and C.O. Paiva-Santos, *J. Eur. Ceram. Soc.*, **23**, 887 (2003).
11. S.A. Pianaro, P.R. Bueno, P. Olivi, E. Longo, and J.A. Varela, *J. Mat. Sci.: Mat. Electron.,* **9**, 159 (1998).
12. P.H. Duvigneaud and D. Reinhard, in *Science of Ceramics* (Ceramurgia s.r.l., Faenza, Italy, 1980), Vol. 12, p. 287.
13. M.J. Mendelson, *J. Am. Ceram. Soc.*, **52**, 443 (1969).
14. P. Murugaraj, T.R.N. Kutty, and M. Subba Rao, *J. Mat. Sci.*, **21**, 3521 (1986).
15. F. Fayat and M.S. Castro, *J. Eur. Ceram. Soc.*, **23**, 1585 (2003).
16. A.C. Antunes, S.R.M. Antunes, A.J. Zara, S.A. Pianaro, E. Longo, and J.A. Varela, *J. Mater. Sci.*, **37**, 2407 (2002).
17. R. Parra, M.S. Castro, and J.A. Varela, *J. Eur. Ceram. Soc.*, **25**, 401 (2005).
18. M.M. Oliveira, P.C. Soares Jr., P.R. Bueno, E.R. Leite, E. Longo, and J.A. Varela, *J. Eur. Ceram. Soc.*, **23**, 1875 (2003).
19. P. DiNola, F. Morazzoni, R. Scotti, and D. Narducci,*J. Chem. Soc. Faraday Trans.*, **89**, 3711 (1993).
20. G.D. Mahan, *J. Appl.Phys.,* **54**, 3825 (1983).
21. L.G.P. Simões, P.R. Bueno, M.O. Orlandi, E.R. Leite, and E. Longo, *J. Electroceram.*, **10**, 63 (2003).